Heliyon 10 (2024) e37199

Contents lists available at ScienceDirect

Heliyon

journal homepage: www.cell.com/heliyon

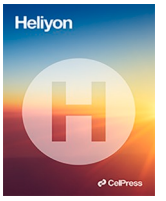

Research article

Investigation of structural, optical, and magnetic properties of $NiFe_2O_4$ for efficient photocatalytic degradation of organic pollutants through photo fenton reactions

Bristy Biswas [*], Md Farid Ahmed, Md Lutfor Rahman, Juliya Khanam, Md Habibur Rahman Bhuiyan, Nahid Sharmin [**]

Institute of Glass and Ceramic Research and Testing (IGCRT), Bangladesh Council of Scientific and Industrial Research (BCSIR), Dhaka, 1205, Bangladesh

ARTICLE INFO

Keywords:
$NiFe_2O_4$
Sol-gel auto-combustion
XRD
VSM
Photocatalysis
Photo-Fenton reactions

ABSTRACT

Nowadays, water pollution generated from textile effluents is one of the major problems for the human race and ecology. Hence, development of sustainable strategies to lower the water pollution level has become a burning need. In this regard, the present study focuses on the preparation of nano catalyst $NiFe_2O_4$ to catalyze the chemical reactions on industrial organic dyes for their fast cleansing from water. By sol-gel auto-combustion technique, $NiFe_2O_4$ nanoparticles were synthesized and exposed to thermal process at temperatures of 400, 600, and 800 °C. Highly crystalline phase with spinel cubic structured $NiFe_2O_4$ was formed with a crystal size of 18.71 nm, which was confirmed by XRD analysis. The FTIR spectra showed two fundamental absorption bands in the range 597.80–412.59 cm^{-1}, which are the characteristics of tetrahedral M − O and octahedral M − O bond in $NiFe_2O_4$. The surface morphology of calcined $NiFe_2O_4$ was investigated by scanning electron microscope (SEM). The nanoparticle size analyzer exhibited that the synthesized $NiFe_2O_4$ nanoparticles had an average particle size of ~ 291.3 nm. Three stage decomposition patterns were observed for $NiFe_2O_4$, which was analyzed by a temperature programmed STA. Zeta potential analyzer showed that the synthesized sample S1 and S2 were stable in the dispersion medium. Also, $NiFe_2O_4$ exhibited optical band gap energies for direct band transitions within the visible spectrum measured to be 1.43–1.45 eV, rendering them effective as photocatalysts under sunlight. The samples showed magnetic measurements by VSM with saturation magnetization, coercivity, remnant magnetization value of 66.81 emu/g, 4.13 Oe and 12.94 emu/g, respectively. The synthesized photocatalyst, $NiFe_2O_4$, at 400 °C, significantly degraded three toxic organic pollutants—Methylene blue, Rhodamine B, and Congo Red—under visible light through 'Photo-Fenton' reaction mechanisms. Among the three dyes, Methylene Blue exhibited the highest degradation percentage with a rate constant of 0.0149 min^{-1} and followed pseudo-first-order kinetic model.

* Corresponding author.
** Corresponding author.
E-mail addresses: bristybiswas065@gmail.com, bristybiswas@bcsir.gov.bd (B. Biswas), sharmin.n6@gmail.com (N. Sharmin).

https://doi.org/10.1016/j.heliyon.2024.e37199
Received 1 June 2024; Received in revised form 28 August 2024; Accepted 29 August 2024
Available online 30 August 2024

1. Introduction

With the rapid industrialization and upgradation in recent years, the versatile uses of hazardous chemical substances excreted from industrial processes tremendously polluted not just the human health but also the environment worldwide [1]. The water sources are constantly being contaminated by different organic hazardous wastes discharges from different industrial effluents. Amongst the several contaminants found in effluents, colorants or dyes are the most vital contaminant which is used globally particularly in the garments, leather manufacturing, and printing industries [2]. According to the World Bank, one-fifth of global industrial water pollution is created from the garments and textiles processing and dyeing [3]. The textile effluents mainly contain cationic and anionic dyes like Methylene Blue (MB), Rhodamine B (Rod B), Congo Red (CR) and so on. These dyes are non-degradable, toxic, tenacious, and significantly degrade water quality even at a very low concentrations [4] leaving an adverse and necrotic effect on the human health [5], as well as other living organisms, and the natural environment. So, the decline in the quality of useable water issues is widely introduced [2,6,7]. To remove these extremely poisonous organic dyes and hazardous contaminants from aquatic sources, different strategies and advanced techniques have been explored including ozonization, biodegradation, adsorption [8,9], chemical oxidation [10], photocatalytic degradation [1,11–13], and membrane filtration [14]. However, all these methods are of high cost, low capability and also produce secondary pollutant. But photocatalysis is considered as a promising, versatile, stable, less energy consuming and highly efficient advanced oxidation technique which uses sunlight supported by a catalyst for the complete decompose of hazardous dyes into CO_2 and H_2O in an environmentally friendly way without any byproduct formation [15–19]. To develop photocatalytic materials which has a high-efficiency, low-cost and advanced oxidation procedure for wastewater treatment is the main focus of this research.

Among the semiconductor-based catalysts used recently for dye degradation, e.g., metal/metal oxides/ferrites/metal composite/nitrides/sulfides etc. [20], ferrites have achieved significant attention for a variety of reasons, making them predominantly attractive for their green environmental-friendly wastewater treatment application [21].

It is reported by many researchers that, TiO_2, ZnO_2, and several noble metal nanoparticles function as excellent catalysts because of surface plasmon-driven catalysis [22–24]. However, TiO_2, ZnO_2 have wide band gap energies, limited capacities to absorb light, and fast recombination of photo-excited electrons and holes. Moreover, as catalysts, noble metal nanoparticles are not yet financially viable. Herein ferrites have proved to be the potent catalysts for photocatalysis reactions for the degradation of organic pigments, colorants, dyes, and others detrimental chemicals because of their size-dependent characteristics with enhanced stable nature, narrow optical band gap energy, recyclability, high adsorption behavior, catalytic activity, and magnetic property [25–29]. There are four types of ferrites namely spinel, garnet, ortho and hexagonal ferrites, based on crystal structures. Among these, spinel ferrites (MFe_2O_4 where, M stands for Mn, Zn, Fe, Co, Ni etc.), are highly valued by the scientists and researchers because of to their size dependent crystalline and anisotropic magnetic nature, excellent enduring stability and magnetic separation [30,31] accompanied by numerous applications such as magnetic storages and devices, gas sensors, photocatalysis, wastewater treatment, lithium-ion batteries etc. [32–34].

Amongst spinel ferrites, Nickel ferrite ($NiFe_2O_4$) which is one of the multifaceted and technologically significant soft ferrite materials have been considered especially for their biocompatibility, recoverability, high catalytic efficiency, high abundance, narrow band gap, strong photo-sensitivity, high electrical resistivity, curie temperature and electrochemical stability as well as ecofriendly nature. However, nickel ferrite finds various uses across different applications such as water purification, enhanced catalysis and photocatalysis, gas-sensor, magnetic storages and devices, delivery of drug, MRI, microwave devices, etc. [35].

Nickel ferrite possess an inverse spinel structure comprising eight-units of $NiFe_2O_4$, where Fe^{3+} and Ni^{2+} ions both occupy the tetrahedral positions, and equivalent number of Fe^{3+} ions fill the tetrahedral positions, generating ferromagnetism [36]. Electrons transferred from Fe^{2+} - Fe^{3+} are accountable for the conduction, and Fe^{2+} give rise to n-type actions and while transfer of holes from Ni^{3+} - $Ni^{2+,}$ and Ni^{3+} are accountable for conduction as well as p-type actions [37]. As such, photocatalysts with recyclable and magnetically separable characteristics have gained great attraction in current study. Two types of photochemical reactions occur at the metal oxides surface, i. e. the oxidation occurs in positive holes, while negative electrons are generated by the reduction produces [38].

Different synthesis procedures have already been developed for the fabrication of nanocrystalline $NiFe_2O_4$, including ball milling, co-precipitation, aerosol route, hydrothermal, solvo-thermal, citrate precursor, microwave, mechano-chemical, reverse micro emulsion technique, sol-gel, and combustion methods, [39]. Among the procedures, sol-gel auto combustion method is greatly important owing to its beneficial promising characteristics such as fast production rate with low temperature, formation of high purity products with good yield, low manufacturing cost, easy synthesis process and with tunable synthesis conditions [40].

The effect of changing divalent cations in nickel ferrite has been described by many researchers in the literature [41–43]. Mahnaz et al. reported the removal of direct red 264 dye using pure and Zn-doped $NiFe_2O_4$ [44]. Differences in the photocatalytic activity of $NiFe_2O_4$ nanomaterials with same composition was described by Dhiman et al. [45]. Degradation of Rhodamine B by oxalic acid-assisted nickel ferrite was studied by Liu et al. [46]. Besides, numerous reports on temperature effect on photocatalytic efficiency of many organic dyes showed the reduction of the photo degradation efficiency with the increase of calcination temperature. Same type results were found in $CuFe_2O_4$, $CoFe_2O_4$, and $ZnFe_2O_4$, emphasizing the crystallite size, surface area and band gap energy [47–49]. Whereas, higher photocatalytic activity of $CoFe_2O_4$ toward methylene blue with increasing annealing temperature from 300 to 400 °C and then lower was confirmed by Swathi et al. [50].

In the present work, microstructural, morphological, optical, and magnetic properties of nickel ferrite synthesized via self-ignited sol-gel method at distinct temperatures was reported and analyzed by means of different characterization techniques. The photocatalytic efficiency of the as-prepared nanoparticles was also studied against Methylene Blue, Rhodamine B and Congo red dyes.

2. Experimental techniques

2.1. Materials

All the chemicals used in this experiment nickel nitrate-hexahydrate [$Ni(NO_3)_2.6H_2O$], ferric nitrate-nonahydrate [$Fe(NO_3)_3.9H_2O$], and citric acid ($C_6H_8O_7$), liq. NH_3 were procured from Merck, Germany with 98 % purity and used without further purification. For photocatalytic dye degradation experiment, two basic dye Methylene blue ($C_{16}H_{18}ClN_3S$, molar mass: 319.85 g/mol) and Rhodamine B ($C_{28}H_{31}ClN_2O_3$, molar mass: 479.02 g/mol) and an azo dye Congo red ($C_{32}H_{22}N_6Na_2O_6S_2$, molar mass: 696.665 g/mol) of analytical grade were used. During the experiments, laboratory produced deionized (DI) water was used.

2.2. Method

In a bottom-up sol-gel auto combustion process, nickel nitrate and iron nitrate were weighed stoichiometrically in an electronic balance and added with 100 mL DI water. The salt solutions were combined homogeneously and stirred continuously with a magnetic stirrer for 30 min, keeping the temperature at 75 °C. A solution of citric acid, which is a chelating agent, was added to the above solution in a 1:1 ratio and the mixed solution was kept stirring at 80 °C for 2 h. Liquid NH_3 was added unless it produced a thick gel-type material. After that, the temperature was increased to 200 °C to dry the gel which in turn burnt out in an auto combustion way producing loose powders, ash. And finally, the resultant black loose ash powders were collected, grinded and exposed to heat treatment at distinct temperatures starting from 400, 600, and 800 °C for 1 h. After the calcination, the final product was collected and categorized as S1, S2, and S3. The synthesis procedure of $NiFe_2O_4$ is represented in Fig. 1.

2.3. Characterization techniques

The powder X-ray diffraction patterns of the fabricated materials were recorded out by Rigaku Smart Lab SE, Diffractometer from Japan operating with a Cu-Kα radiation source of 0.15406 nm, a 2θ range of 10°–80° with 10°/min scan speed to identify the crystal structure and phase composition.

The infrared spectra of the as-prepared samples were investigated by Shimadzu IRAffinity-1S, MIRACLE 10 FTIR spectrometer from Japan and the analysis was conducted using KBr pellets within a wavenumber range from 400 to 4000 cm^{-1} at room temperature.

A simultaneous thermal analyzer NETZSCH STA 449 F5 from Germany was used to perform the thermo-gravimetric (TG) analysis, accompanied by differential scanning calorimetric (DSC) analysis with 10 °C/min heating rate from RT to 1000 °C under N_2 atmosphere.

To investigate the stability of nanoparticles dispersed in aqueous media, the zeta potentials of the synthesized nano nickel ferrites were measured by HORIBA nano Partica SZ-100-S2, Nanoparticle Analyzer from Japan. For sample preparation, 5 mg of as-prepared $NiFe_2O_4$ powders were dissolved in 50 mL of DI water and disseminated for 30 min through an ultrasonic homogenizer.

To estimate the particle size, HORIBA nano Partica SZ-100-S2, Nanoparticle Analyzer from Japan was used where the particle size distribution was observed in the liquid environment using dynamic light scattering method.

To determine the optical band gap energy and reflectance of the synthesized samples, the DRS spectra were measured by PerkinElmer Lambda 1050^+, UV–visible Spectrophotometer from UK.

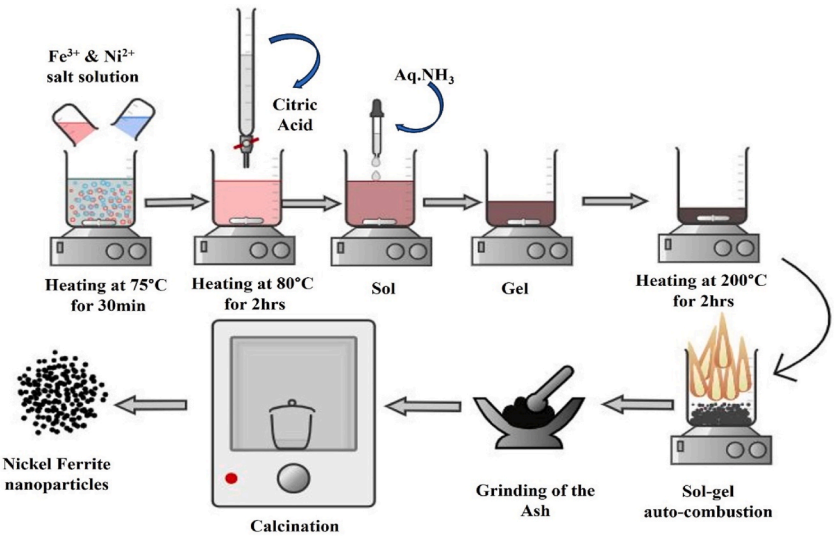

Fig. 1. The pictorial presentation of the synthesis process of $NiFe_2O_4$ nanoparticles by auto-ignited sol-gel method.

The magnetic characteristics and different parameters of the as-prepared nickel ferrite samples were measured by Lakeshore 8604 System, Vibrating Sample Magnetometer (VSM) from USA with an applied magnetic field of +15 k Oe to −15 k Oe at room temperature.

2.4. Procedure for photocatalytic degradation

The photocatalytic activity of the sample S1 was studied against the degradation of MB, CR, and Rod B dyes to evaluate the degradation performance of the material. These time-dependent absorbance spectra of CR, MB, and Rod B degradation were recorded by Hitachi UH5300, UV–Vis spectrophotometer from Japan in the range 400–800 nm and represented by Fig. 2(a–d). The natural solar light irradiation from 11.00 a.m. to 3.00 p.m. of the day was used to explore the photo degradation efficiency of $NiFe_2O_4$ with addition of 1 mL of 30 % H_2O_2.

To undergo the experiment, in a 100 mL of the 10 ppm of the aqueous dye solution, 0.05 g catalyst was added. After that, the mixer was reserved in the dark with continuous stirring for 30 min to attain the adsorption and desorption equilibrium between the photocatalyst and dye molecule. Next, the reaction mixture was irradiated by sunlight with continuous stirring. At a fixed periodic time, 5 mL solution was taken out from the beaker and the decrease in dye's color and the dye concentration (absorbance) was determined by UV–Visible spectrophotometer. Finally, the photocatalytic efficiency was calculated using the following Eq. (1),

$$\text{Efficiency } (\%) = \frac{C_0 - C_t}{C_0} \times 100 \tag{1}$$

here, C_0 = Concentration of dye with catalyst at 'zero' time.

C_t = Concentration of dye with catalyst after 't' time.

To study the reaction kinetics of nickel ferrite against CR, MB, and Rod B, pseudo-first-order kinetic model was evaluated as follows Eq. (2) [52].

$$C_t = C_0 e^{-kt} \tag{2}$$

where k is called the pseudo-first-order rate constant (L min^{-1}).

By taking logarithm on both sides, Eq. (2), results in:

$$-\ln \frac{C_t}{C_0} = kt \tag{3}$$

From Eq. (3), considering the linear fitting curve between ln (C_t/C_0) and time (t), along the Y-axis and X-axis respectively, and

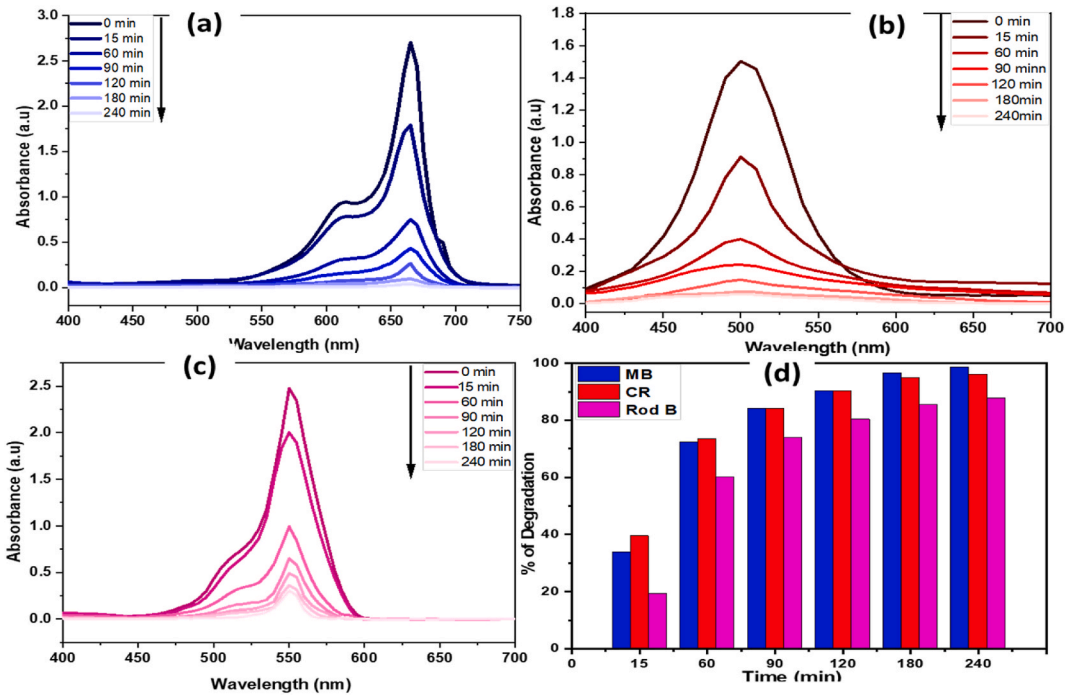

Fig. 2. Chronological UV–vis spectra of $NiFe_2O_4$ for (a) MB, (b) CR, (c) Rod B, and (d) Comparison of degradation percentage vs time among MB, CR and Rod B.

comparing with the straight-line eq. y = mx + C, the negative slope of the fitted line is obtained which is equivalent to 'k'. So, these reactions were first-order (Fig. 14(b). The adsorption capacity of the synthesized photocatalyst was calculated using following Eq. (4) [51].

$$q_e = \frac{V(C_0 - C_t)}{W} \tag{4}$$

3. Results and discussion

3.1. Crystallographic analysis (XRD)

The X-ray diffractograms of the prepared $NiFe_2O_4$ samples labeling as S1, S2, and S3 at sintering temperature 400, 600 and 800 °C are represented in Fig. 3. The X-ray diffraction pattern shows distinct peaks at 2θ values of 18.38°, 35.69°, 37.36°, 43.38°, 53.81°, 57.38°, 62.99°, 71.50° 74.58°, and 75.54° which are the characteristic peaks of $NiFe_2O_4$ and reflected from planes with miller indices (111), (220), (311), (222), (400), (422), (511), (440), (620), (533) and (622), respectively. Cubic spinel structures of $NiFe_2O_4$ with was confirmed by these peak positions which were highly consistent with the standard spectrum of $NiFe_2O_4$ according to JCPDS standard card no. 10–0325 [52].

With the gradual increment of the calcination temperature, the relative intensity of the peaks rises gradually, indicating improved crystalline nature of synthesized $NiFe_2O_4$ samples [49,53]. The factor may be attributed to the grain growth of the particles in the nano-region to reduce the surface energy and higher temperatures favored the activation energy required for nucleation by lowering it [54].

The sample calcined at 400 °C displayed widened peaks with significant intensity indicating the cubic spinel phase of $NiFe_2O_4$ with small crystallite size. In case of sample S2 and S3, annealed at 600 and 800 °C, sharper peaks were observed signifying larger crystallite size.

3.1.1. *Structural parameters*

Using the X-ray diffractograms, the crystallite size of the nickel ferrite particles was calculated from Scherrer's formula as Eq. (5) [55,56].

$$D_{C-S} = \frac{k\lambda}{\beta_D \cos\theta} \tag{5}$$

where, $D_{C\text{-}S}$ refers to the crystalline size (nm), k represents a shape-dependent constant with a value of 0.94, and λ denotes X-ray wavelength (λ = 0.15406 nm), β_D corresponds to the peak width at half maximum intensity (FWHM), and θ signifies the diffraction angle based on Bragg's law.

Microstrain (ε), which is the effect of crystal defects, distortion and lattice mismatch in powder sample can be expressed by Stokes and Wilson equation from Eq. (6) [55]

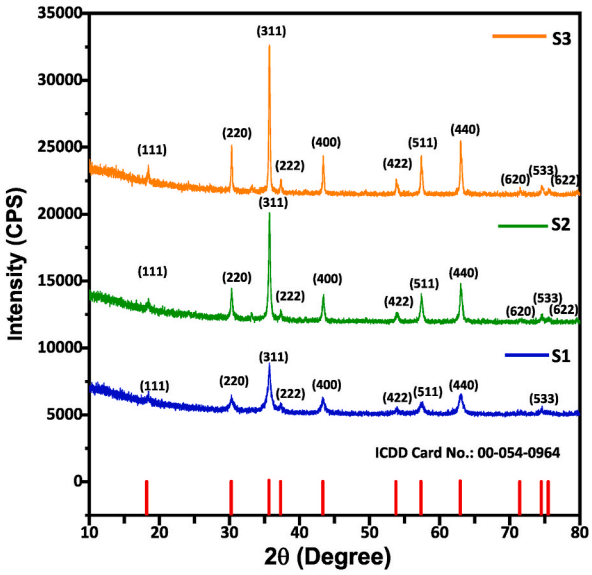

Fig. 3. PXRD patterns of nanocrystalline $NiFe_2O_4$ powders calcined at 400 °C, 600 °C & 800 °C.

$$\varepsilon = \frac{\beta_{strain}}{4\ tan\ \theta} \tag{6}$$

The dislocation density (δ) of nickel ferrite measured from Williamson and Smallman's formula is given by Eq. (7) [56].

$$\delta = \frac{1}{(D)^2} \tag{7}$$

Lattice constant of the nanoparticles 'a' was calculated from the XRD pattern by the following Eq. (8) using Bragg's Law [50].

$$a = d\sqrt{h^2 + k^2 + l^2} \tag{8}$$

here 'a' is the lattice parameter linked with the respective 2θ peak position, and 'd' is the inter-planar spacing. The integers h, k and l are described as Miller indices [55,57]. The cube of the lattice constant "a" is equal to the cell volume [55] which is expressed in Eq. (9).

$$V = a^3 \tag{9}$$

The X-ray density (ρ_x) of nickel ferrite nanoparticles was calculated using the standard relation given by Eq. (10) [57].

$$\rho_x = \frac{8M}{N_A\ a^3} \quad gm \Big/ cm^3 \tag{10}$$

where 'ρ_x' is X-ray density, 'M' is the molecular weight, 'a' is the lattice constant, 'N_A' is the Avogadro's number and '8' is the number of molecules per unit cell. Using Archimedes' principle, the bulk density 'ρ_b' of the fabricated nickel ferrite sample was assessed. The percentage of porosity of nickel ferrite nanoparticles was measured from the following Eq. (11) [57].

$$P = \frac{\rho_x - \rho_b}{\rho_x} \times 100\ \% \tag{11}$$

The deduced values of crystallite size (D), strain ($\boldsymbol{\varepsilon}$), lattice parameter (a), volume of the unit cell (V), dislocation density (δ), X-ray density (ρ_x), bulk density (ρ_b), percentage of porosity (P) of the synthesized $NiFe_2O_4$ particles sintered at different temperatures is shown in Table 1.

Fig. 4 represents the increase of crystallite size as well as lattice parameter with calcination temperature for the nickel ferrite samples. The lowest crystallite size is 18.71 nm at 400 °C with 8.3334 Å lattice constant and the highest one is 51.52 nm at 800 °C having a lattice constant of 8.3360 Å.

From Table 1, it is clear that the density of X-ray and percentage of porosity in $NiFe_2O_4$ samples decrease with the rising of calcination temperature while the lattice constant, unit cell volume and bulk density increase. As particles grow larger with increasing calcination temperature, so the porosity decreases. Bulk density of $NiFe_2O_4$ is less than the X-ray density due to the presence of pores in the sample, both of which are influenced by the annealing process [57].

3.2. FTIR analysis

FTIR spectral analysis of the investigated $NiFe_2O_4$ samples of calcination temperatures 400, 600 and 800 °C have been performed to confirm the formation of spinel structure in nickel ferrite which are depicted in Fig. 5. From the spectra, it is clearly seen that there are two main broad metal–oxygen bands are present in the wavenumber ranging from 4000–400 cm^{-1} which are the characteristics for all spinel materials, particularly ferrites. The higher frequency band (ν_1) detected in the range 600–550 cm^{-1}, results from the stretching vibrations of tetrahedral metal–oxygen (M_{tet}-O) bond, whereas the lower band (ν_2) is normally observed in a wavenumber of 450–385 cm^{-1}, which is arised from the octahedral metal–oxygen (M_{oct}-O) bond [58]. The observed vibrational modes confirm the presence of spinel $NiFe_2O_4$ phases in all samples. The tetrahedral (ν_1) and octahedral (ν_2) bands are tabulated in Table 2. According to Table 2, the bands associated with ν_1 and ν_2 shift toward higher wavenumbers with increasing calcination temperature, which can be ascribed to the development of crystallinity of the samples, grain size, with the increase in annealing temperature [54].

Table 1
Effect of calcination temperature on structural parameters.

S. Id	CT (°C)	Crystallite Size, D (nm)	Strain, $\boldsymbol{\varepsilon} \times 10^{-3}$	Dislocation density, $\delta \times 10^{14}$ (lines/m^2)	Lattice constant, a, (Å)	Unit cell volume V, $(Å)^3$	X-ray density, ρ_x (g/cm^3)	Bulk density, ρ_b (g/cm^3)	Percent porosity, P (%)
S1	400	18.71	6.04	28.57	8.3334	578.71	5.3821	4.4181	17.91
S2	600	39.18	2.88	6.51	8.3353	579.12	5.3783	4.6844	12.90
S3	800	51.52	2.19	3.77	8.3360	579.26	5.3770	4.7366	11.91

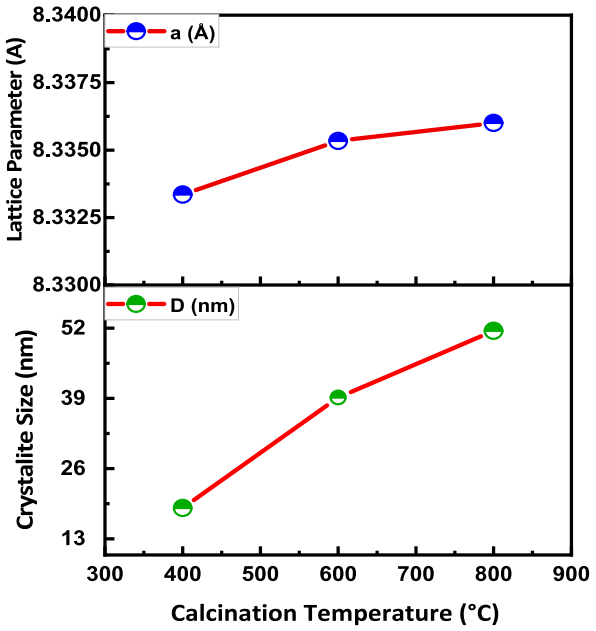

Fig. 4. Variation of crystallite size and lattice parameter with calcination temperature.

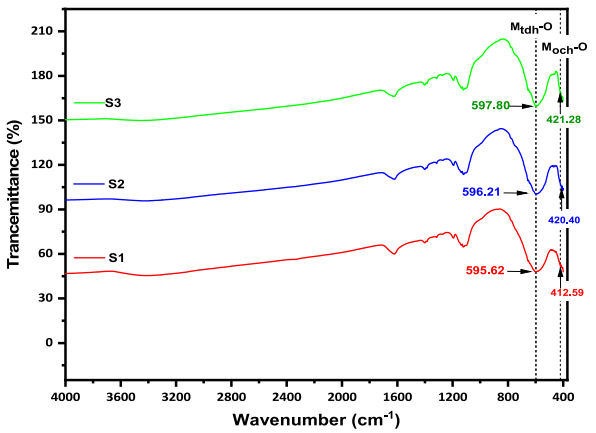

Fig. 5. FTIR spectrum of the synthesized samples (S1, S2 and S3).

Table 2
FTIR bands of $NiFe_2O_4$ sample.

Preparation technique	Temperature, °C	IR bands (cm^{-1})	
		ν_1	ν_2
Sol-gel auto combustion	400	412.59	595.62
	600	420.40	596.21
	800	421.28	597.80

3.3. Morphological analysis

The morphology and texture of the prepared powdered nickel ferrite samples calcined at three distinct temperatures were examined by SEM, which are displayed in Fig. 6. The SEM micrographs revealed that the resultant nano crystallites which are smaller grains-like particles were of irregular shape, dense surfaces and huge agglomeration [55]. Since the particles are huge clustered, so the concrete particle size as well as distribution from SEM analysis was not possible. The degree of agglomeration of $NiFe_2O_4$ samples increased as the calcination temperature due to the increased surface energy of $NiFe_2O_4$ nanoparticles having high surface area as well

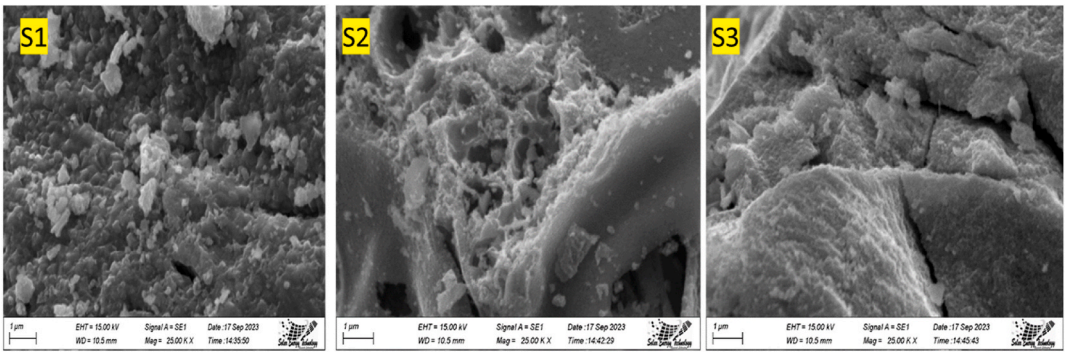

Fig. 6. SEM micrographs of $NiFe_2O_4$ samples (S1, S2, and S3).

as strong magnetic dipole-dipole interactions among the nanoparticles and leading to large particle size [59]. Consequently, the porosity of the samples was decreasing with increasing temperature which was in agreement with the results recorded in Table 1 [57].

3.4. Nanoparticle size analysis

At the room temperature (25 °C), the sizes of the particles as well as size distribution for $NiFe_2O_4$ powders in colloidal solutions was measured by nano-particle size analyzer which are shown in Fig. 7. Table 3 summarized that the $NiFe_2O_4$ nano particles are poly dispersed with a diameter of 291.3 nm–393.8 nm for the samples calcined at 400 °C and 800 °C respectively.

The mean particle sizes of the prepared $NiFe_2O_4$ particles have increased as the calcination temperatures rises which are in consistent with the results from XRD. As DLS method measures the hydrodynamic diameter of a particle arised from Brownian motion, that's why the hydrodynamic diameter obtained from Nanoparticle Analyzer is always bigger from the desiccated diameter from SEM micrographs [57].

3.5. Thermal stability

To observe the structural decomposition of the intermediate product, such as the weight loss, evaporation, phase transformation, etc. during the thermal course, resulting from the sol-gel auto combustion method, thermo-gravimetric analyzer was used with a ramping rate of 10 °C/min which are depicted in Fig. 8(a) [60]. A substantial mass change of 1.28 % was occurred from room temperature to around 210 °C, due to loss of interstitial water, accompanied by an endothermic peak in the DSC curve within the region as shown in Fig. 8(b). A steep decline of weight loss of 3.20 % was seen in the range of 210–425 °C, as a result of the evaporation of CO_2, led to an exothermic peak in the DSC. Weight loss occurred between 400 and 1000 °C as a consequence of structural change to $NiFe_2O_4$. The conversion of spinel phase of $NiFe_2O_4$ was occurred at temperature 541.1 °C, confirmed by an exothermic peak in DSC. The residual mass of $NiFe_2O_4$ was 95.04 %.

3.6. Zeta potential analysis

The zeta potential, a very important parameter for colloidal dispersions, measures the electrostatic attractions and repulsions between particles in a solvent. Fig. 9 demonstrates the results for all synthesized $NiFe_2O_4$ samples in liquid medium with neutral pH, exploring the electrical potential of the nanoparticles. It is already established that samples possessing zeta potential value above +30 mV or below −30 mV, are considered as the stable particles in the dispersion medium.

The obtained data demonstrates that the samples S1 and S2 display a high level of steadiness in the solvent with zeta potential value

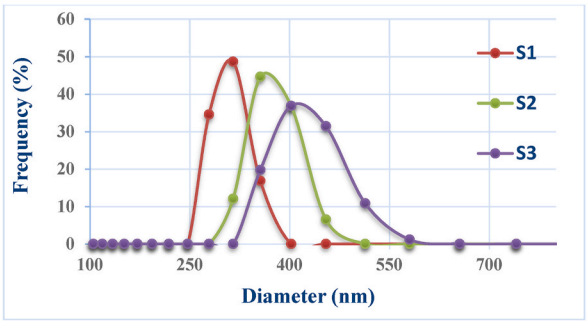

Fig. 7. Nanoparticle size distribution $NiFe_2O_4$ samples (S1, S2 and S3).

Table 3
Particle size distribution results of synthesized $NiFe_2O_4$ particles.

Sample ID	Average Particle Size (nm)
S1	291.3
S2	352.5
S3	398.8

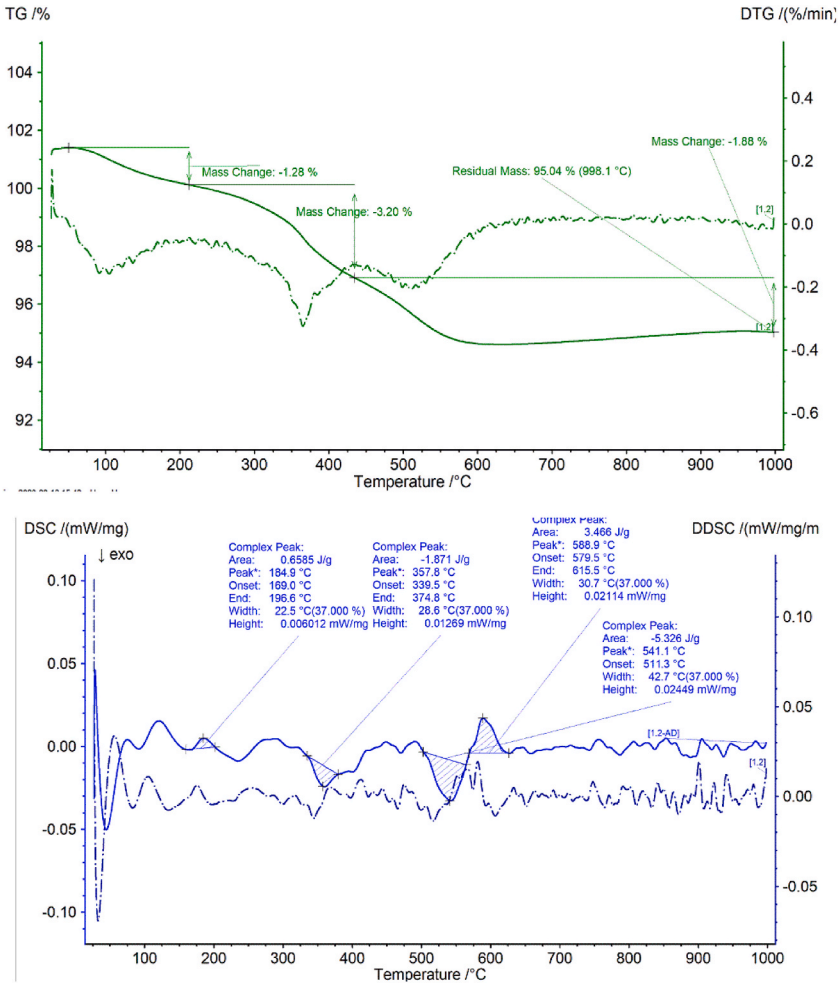

Fig. 8. (a) TG and **(b)** DSC graph of $NiFe_2O_4$ intermediate.

of −36.5 mV and −38.8 mV while the sample S3 possess the zeta potential value of −23.1 mV being unstable in the dispersion medium.

3.7. Optical properties

3.7.1. Absorbance and band gap energy

To reveal the optical properties of $NiFe_2O_4$ nano structures, UV–Visible spectroscopy was used. Diffuse reflectance spectroscopy (DRS) method accompanied by Kubelka-Munk function which is employed mainly for investigating powder samples was used for estimation of the optical band gap energies (E_g) of the obtained samples. Fig. 10(a–b) illustrated the percentage of reflectance (R) and absorbance (K-M) as a function of wavelength (λ) for the $NiFe_2O_4$ powder samples at different temperatures in the visible range of 400–800 nm. All the nanoparticles exhibited significant reflectivity and broad absorption bands in the range of 400–800 nm and the significant increase of intensity of the peak in the red region (620–780 nm) with the rise of calcination temperatures suggests their application in photocatalysis and other optical devices [59,61].

In general, the energy required for electrons to transit from the valence band to the conduction band is known as band gap energy

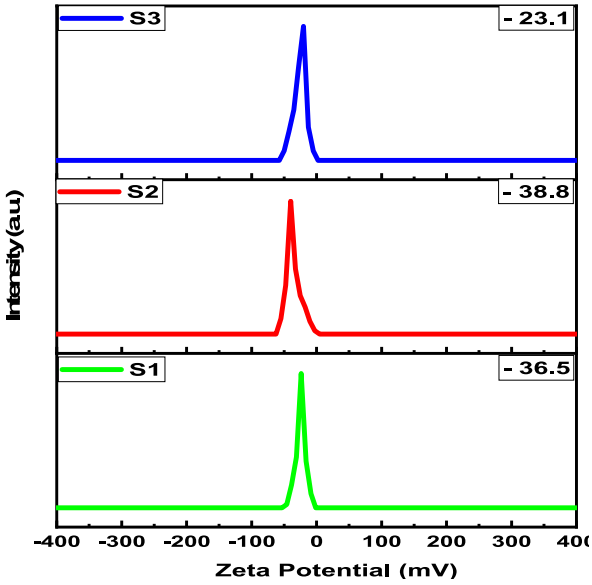

Fig. 9. Zeta potentials of $NiFe_2O_4$ nanoparticles (S1, S2 and S3) at different calcination temperatures.

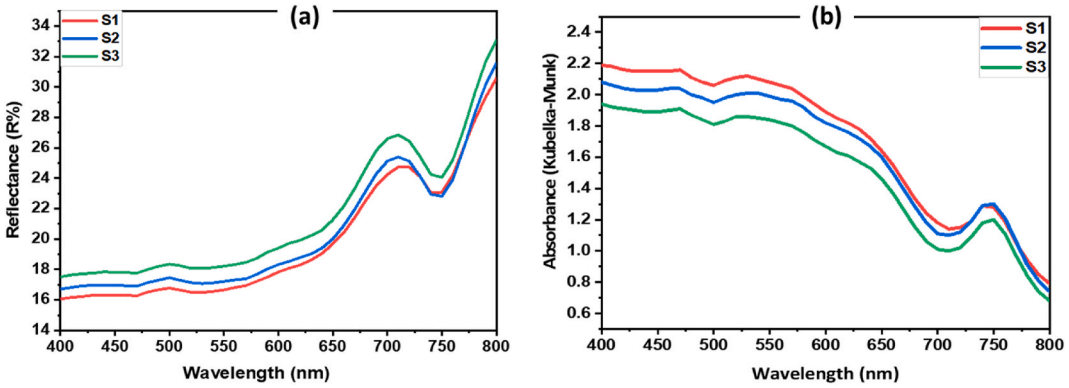

Fig. 10. UV–Visible **(a)** reflectance (R) spectra and **(b)** absorbance (Kubelka-Munk) spectra.

and is directly proportional to the band gap of ferrites [45]. Therefore, the 2p valence band of O and 3d conduction bands of Fe in $NiFe_2O_4$, can be attributed for this electronic transition in the DRS response [54].

Thus, the Kubelka-Munk (K-M) function, related to the absorption coefficient is expressed as follows Eq. (12):

$$F(R) \equiv \alpha = \frac{(1-R)^2}{2R} \tag{12}$$

where, F(R), α, and R stand for Kubelka-Munk function, material's absorption co-efficient and reflectance. A relationship between α and *Eg* is given by the Tauc plots as follows Eq. (13),

$$\alpha h\upsilon = A\left(h\upsilon - E_g\right)^n \tag{13}$$

By replacing α by *F*(*R*), and therefore, eq (13) can be written as follows Eq. (14),

$$F(R)\, h\upsilon = A\left(h\upsilon - E_g\right)^n \tag{14}$$

where A = proportionality constant, hυ = photon energy, and E_g = optical band gap energy. The exponent n can take a value of 2 or ½, depending on the nature of electronic transition. Usually, *n* is considered as 2 for indirectly allowed transition, while *n* is 1/2 for directly allowed transition. As spinel ferrite possess a direct band gap (n = 1/2) [60], hence Eg is determined from the linear absorption edge part with the energy axis of the graph $(\alpha h\upsilon)^2$ vs hυ, as illustrated in Fig. 11. The difference of the estimated values of E_g for nickel ferrite nanoparticles as an extent of the calcination temperatures is given in Fig. 11 which clearly shows a decreasing trend with

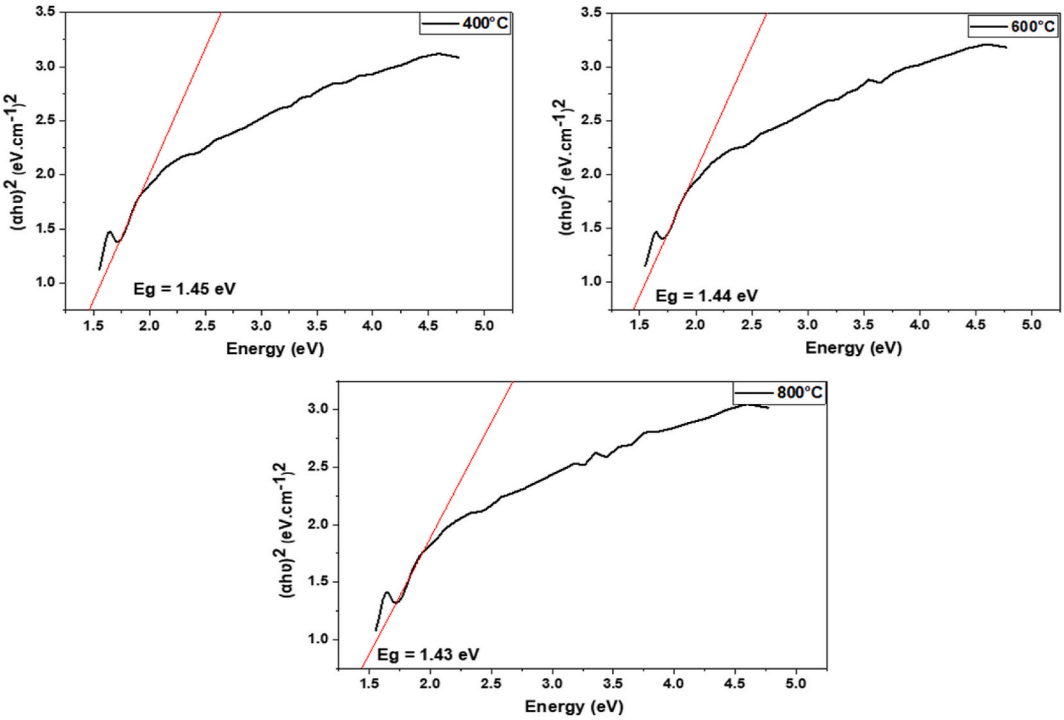

Fig. 11. The optical band gap energy of $NiFe_2O_4$ nanoparticles.

increasing crystallite size.

3.8. Magnetic studies

Fig. 11 shows the room temperature (25 °C) dependence of the magnetization M (emu/g) of $NiFe_2O_4$ nanoparticles with the help of applied magnetic field H (Oe) of −15 to 15 K Oe i.e. M − H hysteresis loops, investigated by vibrating sample magnetometer (VSM). The M − H curve (Fig. 12) indicates that all these nanoparticles exhibit the ferromagnetic behavior. Different magnetic parameters like saturation magnetization (*Ms*), remanent magnetization (*Mr*), coercivity (*Hc*) and squareness ratio (*Mr*/*Ms*) obtained from the hysteresis curve are summarized in Table 4.

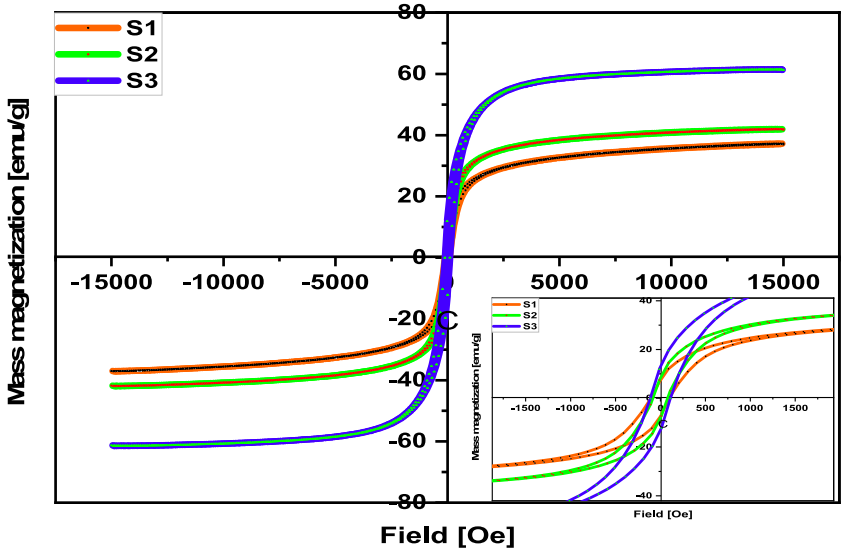

Fig. 12. M − H loops of nanocrystalline $NiFe_2O_4$ powders prepared from self-ignited sol-gel method.

Table 4
Magnetic parameters of $NiFe_2O_4$ nanoparticles measured from VSM at room temperature.

Sample ID	Ms (emu/g)	Hc (Oe)	Mr (Oe)	K	Mr/Ms	η
S1	40.06	1.4	7.37	58.421	0.184	1.681
S2	44.98	1.76	8.1	82.463	0.180	1.888
S3	66.81	4.13	12.94	287.422	0.194	2.804

The obtained saturation magnetization as well as coercivity for $NiFe_2O_4$ nanoparticles show a consistent rise in temperature as the sintering temperature increases, similar to the recent studies [62,63], which can be explained by some aspects for example; particle size, grain growth, domain structure, and cations distributions between tetrahedral and octahedral sites during the calcination process [63,64]. However, a big magnetic particle possesses a multiple domain structure abide by domain walls that divide the areas of consistent magnetization. The development of domain wall is dynamically favored when the energy needed to generate a domain wall is smaller than the variance between the magneto-static energies of the single-domain and multi-domain states [54]. Therefore, in this circumstance, the particle size as well as coercivity is increased to extent of increasing sintering temperature.

Moreover, the squareness ratio ($S = Mr/Ms$), used to evaluate the inter- and interexchange interactions between grains was also estimated using the hysteresis loop, According to Stoner and Wohlfarth's theory, particles are non-interacting and randomly oriented when the squareness ratio S equals 0.5, while S is less than 0.5 for particles reacting via magneto-static interactions [60]. In this work, S is quite lower than 0.5 for all samples, signifying magneto-static actions as well as single domain nature of the synthesized $NiFe_2O_4$ samples, thereby supporting the growing tendency of coercivity with the growth of particle size owing to increased calcination temperature.

The values of magnetic moment (η_B) per formula unit in Bohr Magneton (μB) and magnetic anisotropy (K) of as-prepared samples were also calculated using the following Eq. (15) and Eq. (16) [59].

$$\eta_B = \frac{MW \times M_s}{5585} \tag{15}$$

$$K = \frac{M_s \times H_c}{0.96} \tag{16}$$

Here, the molecular weight of the sample is denoted as MW and Ms is the saturation magnetization.

4. Application studies

4.1. Photocatalytic activity

The photocatalytic performance of nickel ferrite to breakdown organic harmful dyes was tested using MB, Rod B and CR dyes under sunlight irradiation. Here nickel ferrite nanoparticles with the lowest band gap energy was chosen to perform the experiment as the electron (e^-)-hole (h^+) generation would be easier in this sample than the others samples. The catalytic breakdown of MB, Rod B and CR dyes was performed at 32 ± 2 °C temperature under the sunlight with addition of 1 mL 30 % H_2O_2. There are several parameters that affect the degradation process. Among them, the amount of catalyst to be used for photocatalytic experiments was optimized with catalyst dosages ranging from 0.025 g to 0.075 g and keeping the dye concentration fixed at 10 mg/L for 240 min. With the increase of catalyst amount, the percentage of MB, Rod B, and CR degradation increased which is represented in Fig. 13 [56].

For MB, the maximum degradation percentage was found for 0.05 g catalyst, which was 0.075 g for both Rod B and CR dyes.

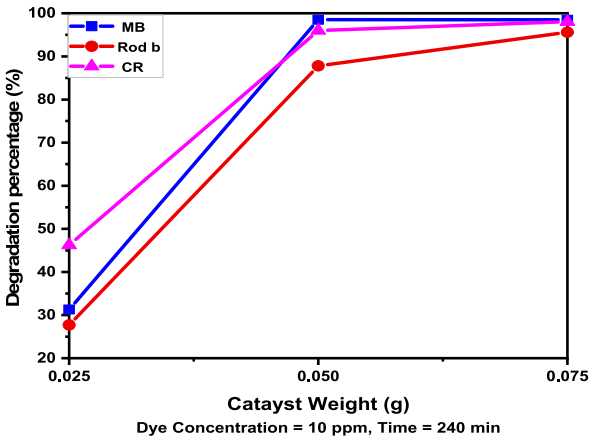

Fig. 13. Variation of degradation percentage with catalyst amount.

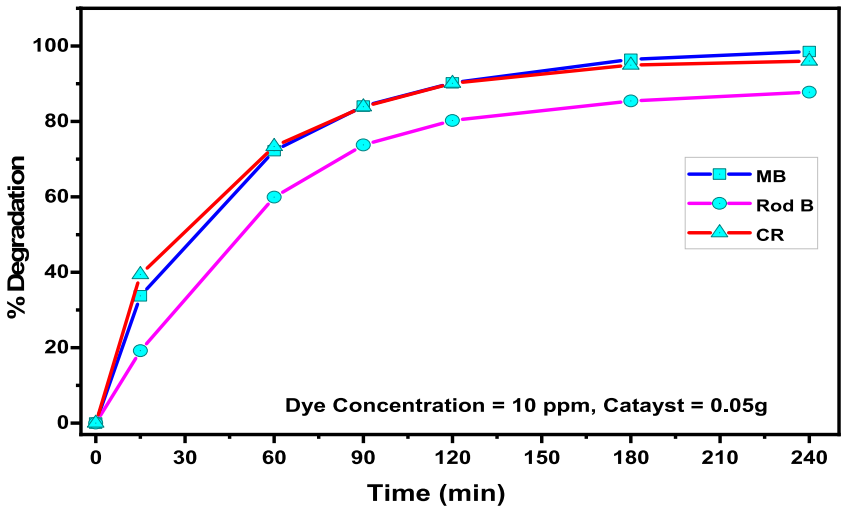

Fig. 14. Time dependent degradation efficiency graph between MB, Rod B and CR.

However, the catalytic effectiveness of 0.075 g $NiFe_2O_4$ against 10 ppm Rod B and CR dyes is not significant compared to 0.05 g. The results suggest that at this particular concentration of dyes, the catalytic activity of the $NiFe_2O_4$ catalyst is most efficient when using 0.05 g of the catalyst material. So, the optimal catalyst weight for 10 ppm dye concentration was determined to be 0.05 g.

The percentage of degradation of the MB, RhB, and CR dyes using synthesized $NiFe_2O_4$ nanoparticles are represented in Fig. 14. While carrying out the reactions, a hypochromic shift was noted with time, for each of the three mentioned dyes, indicating the decrease in the absorbance as well as concentration of MB, CR, and RhB [65]. The CR dye's degradation rate was initially faster than the other two dyes. But, after 90 min, the catalyst S1 degraded more MB dye than Rod B and CR and continued the trend till the end. Around 90.22 % of MB and 90.09 % of CR dye was degraded within 120 min, while it was 80.20 % for Rod B. The degradation percentage of Rod B was found not to change significantly from the other two dyes from the very beginning. The spectra displayed that the complete decomposition of MB, CR, and RhB dyes against the S1 sample was achieved in 240 min of natural solar light irradiation, which was calculated to be 98.51 %, 95.99 %, and 87.80 %, respectively.

The catalytic effectiveness of $NiFe_2O_4$ was found to be the maximum for MB dye among the three dyes confirming that the degradation of MB depends extremely on what type of catalyst is used. As the photocatalytic activity depends mainly on the electron-hole (e^-/h^+) pairs production through band gap upon visible light radiation, inducing a redox process with dye molecules adsorbing on the photo catalyst's surface. In this experiment, the synthesized nickel ferrite sample (S1) has a narrow band gap energy compared to the bulk one (2.2 eV) [65]. The increased surface area of S1 was induced and governed from surface to volume proportion of the nano-size of the studied sample, which has made $NiFe_2O_4$ a more potential candidate in organic dye removal from wastewater.

4.2. Stability and recovery studies

The synthesized photocatalyst was chosen to evaluate the recycle and recovery experiments against MB dye which are considered as the first condition for any catalyst. Being magnetic catalyst, $NiFe_2O_4$ nanoparticles were easily recovered each time after MB photo degradation process to carry out the recycling experiment. Every cycle involved separating the suspension from the solution using an external magnetic field, followed by repeatedly washing with ethanol and distilled water, and finally dried in the oven [65]. Following the same steps mentioned above, the recovered photocatalyst was employed for three times to breakdown MB as a model in order to examine the photostability and reusability of the as-prepared photocatalyst. The degradation efficiency in three successive days were 98.51 %, 96.32 %, and 93.57 % respectively. As demonstrated in Fig. 15, there was little change in the degradation percentage which was likely to occur during the recyclability process. Therefore, $NiFe_2O_4$ is found very effective in long-term dye degradation process because of having great stability, magnetic properties and easy recovery process from the catalytic system.

4.3. Chemical kinetics

The kinetic data obtained for MB, Rod B, and CR photodegradation were plotted in coordinates $(C_t/C_0)/t$ and -ln $(C_t/C_0)/t$ and are represented in Fig. 16(a–b). The rate constants values calculated from the slopes of the linear fits and regression coefficient (R^2) are recorded in Table 5.

The values were found to be in the range of 0.95–0.99. As the value of regression coefficient are almost close to 1, so all the degradation processes follow the pseudo-first-order kinetics. The rate constant (k) values for MB, CR, and Rod B degradation reactions with S1 were found to be 0.0149, 0.0135, and 0.0090 min^{-1}, respectively. The S1 sample showed the highest k value in MB with higher regression coefficients (R^2), followed by CR and RhB. To evaluate, it is important to note that the S1 catalyst can degrade MB (19.59 mg g^{-1}) in 240 min while it is 17.15 and 18.68 mg g^{-1} respectively for Rod B and CR dyes.

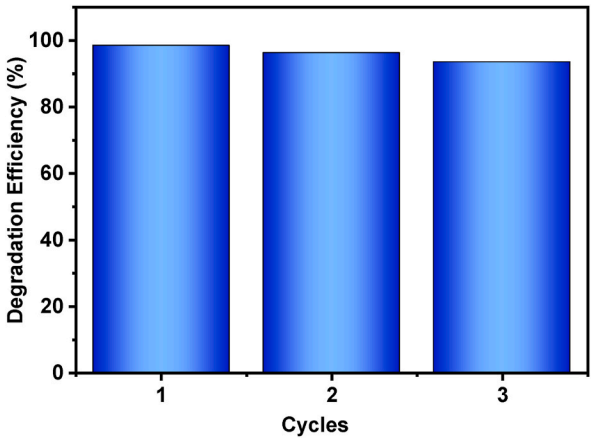

Fig. 15. Reusability of $NiFe_2O_4$ catalyst over three consecutive cycles.

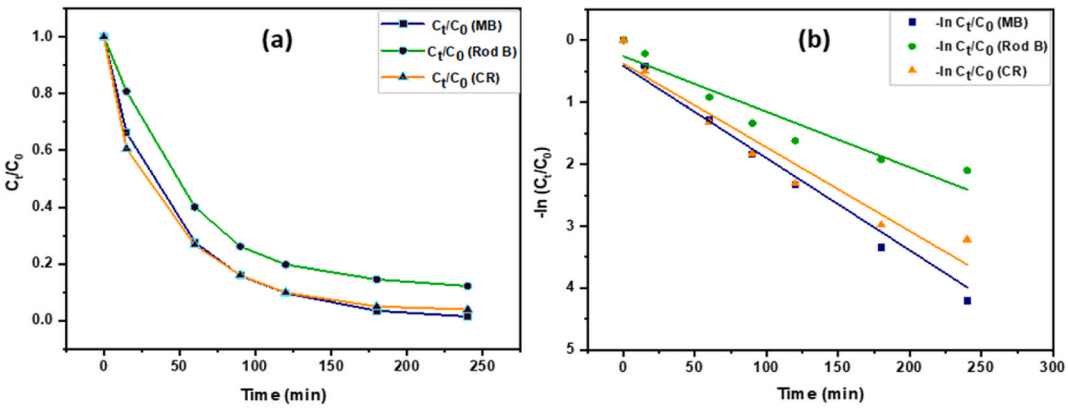

Fig. 16. Kinetics of photo degradation process of MB, Rod B and CR
(a) C_t/C_0 vs. time (b) Pseudo-first-order kinetics of -ln (C_t/C_0) vs time.

Table 5
Kinetic data of photodegradation of $NiFe_2O_4$ nanoparticles.

Photocatalyst	Dye	Time (min)	% Degradation	Reaction Rtae, k (min^{-1})	R^2	q_e (mg/g)
S1	Methylene Blue	240	98.51	0.0149	0.9959	19.59
	Rhodamine B	240	87.80	0.0090	0.9531	17.15
	Congo Red	240	95.99	0.0135	0.9706	18.68

4.4. Active species and possible degradation mechanism insight

As represented in Fig. 17, $NiFe_2O_4$ being a heterogeneous photocatalyst absorb photons having energy above or same as the band gap energy of the catalyst, when exposed to visible light. An electron (e^-) from the valence band (VB) of $NiFe_2O_4$, jumps to the conduction band (CB) leaving a hole (h^+) behind (Eq. (17)). The electrons in the CB interact with the absorbed O_2 in the medium, leading to superoxide radical anion ($\bullet O_2^-$) through a reduction process, which further results in the formation of the potent oxidizer OH• radicals to degrade the dyes by reacting with H_2O_2 or attacking the dye molecules (Eq. (18)–(21)). On the other hand, OH• radicals are also produced from the VB through reactions with H_2O and h^+, which is responsible for degrading dyes (Eq. (22) and (26)). Additionally, the Fe^{3+} ions in $NiFe_2O_4$ can potentially undergo a reaction with H_2O_2 to be reduced to Fe^{2+} which subsequently reacts with H_2O_2 to produce the more potent oxidizing agent OH• [64] (Eq. (24)–(26)). Therefore, hydrogen peroxide (H_2O_2) additionally plays a pivotal role in enhancing the degradation reactions by increasing the concentration of OH· through catalytic decomposition and reduces the recombination time of charge carriers [64]. (Eq. (23)).

From the above-discussed results, all three dyes MB, CR, and RhB were found to be degraded by nickel ferrite; which occurs through Fenton reaction (in the presence of Fe^{3+} and H_2O_2), accompanied by Photo-Fenton reactions (owing to visible light irradiation). Based

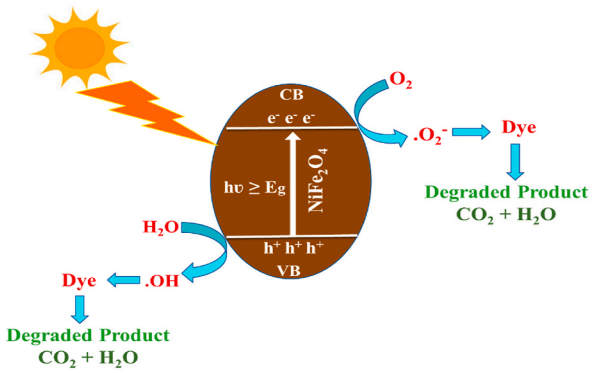

Fig. 17. Photodegradation process of MB, Rod B and CR dyes by $NiFe_2O_4$ under visible light.

on these results from the experiments, a viable mechanism of photo-sensitized catalytic degradation of organic dyes by $NiFe_2O_4$ was deduced (Fig. 17). Initially,

$$NiFe_2O_4 + h\upsilon \rightarrow NiFe_2O_4\left(h^+_{VB} + e^-_{CB}\right) \quad (17)$$

$$H_2O_2 \rightarrow 2OH \quad (18)$$

$$e^- + O_2 \rightarrow \bullet O_2^- \quad (19)$$

$$\bullet O_2^- + Dye\ (MB, Rod\ B\ and\ CR) \rightarrow Degraded\ Products\ (CO_2, H_2O) \quad (20)$$

$$\bullet O_2^- + H_2O_2 \rightarrow OH\bullet + OH^- + O_2 \quad (21)$$

$$h^+ + H_2O \rightarrow OH\bullet \quad (22)$$

$$e^- + H_2O_2 \rightarrow OH\bullet + OH^- \quad (23)$$

$$Fe^{3+} + H_2O_2 \rightarrow Fe^{2+} + H^+ + HO_2^{\cdot} \quad (24)$$

$$Fe^{2+} + H_2O_2 \rightarrow Fe^{3+} + OH^{\bullet} + OH^- \quad (25)$$

Table 6
Comparison of the current research with the literature.

Sample	Synthesis procedure	Dye	Source	Time (min)	Degradation efficiency (%)	Ref.
$ZnFe_2O_4$@ graphene nanosheets	Hydrothermal method	Congo Red	Xenon lamp	240	88.66	[66]
$NiFe_2O_4$@ graphene oxide	Sol–gel auto-combustion method	Methylene Blue	UV lamp	150	90.84	[67]
$NiFe_2O_4$/ZnO	Ultrasonication method	Methyl orange Methylene Blue	Sunlight Sunlight	40 40	49.2 44.40	[68]
$MnFe_2O_4$	Co-precipitation route	Acid violet 7	Visible light	80	49	[69]
$ZnFe_2O_4$	Combustion method	Malachite Green	Visible light	60	64.3	[45]
$MgFe_2O_4$	Co-precipitation route	Methylene Blue	Visible light	240	89.73	[70]
$SrFe_{12}O_{19}$	Chemical co-precipitation	Methylene Blue	Visible light	–	90.2	[71]
$CoFe_2O_4$	Co-precipitation route	acid violet 7 MB	visible light	80	41 81	[69]
$CuFe_2O_4$	Auto combustion	Rhodamine B	Visible light	–	94	[72]
$CaFe_2O_4$	Solution Combustion	Evans blue	Visible light	90	98.11	[73]
$NiFe_2O_4$	*Sol-gel Auto Combustion*	*Methylene Blue* *Congo Red* *Rhodamine B*	*Visible light*	*120, 240* *120, 240* *120, 240*	*90.22, 98.51* *90.09, 95.99* *80.20, 87.80*	*Present work*

$$OH\bullet + Dye\ (MB, Rod\ B\ and\ CR) \rightarrow Degraded\ Products\ (CO_2, H_2O) \quad (26)$$

4.5. Comparative studies

A detailed comparison between photocatalytic activity of $NiFe_2O_4$ of the current research with other ferrites and other nickel ferrites synthesized by other methods has been carried out with the existing literature which include the synthesized material, synthesis procedure, lighting source, time, as well as its degradation efficiency to understand the impacts of current research (Table 6).

5. Conclusion

In current research work, the influence of calcination temperature on the structural, magnetic, optical properties and photocatalytic activity of nano crystalline nickel ferrite particles has been investigated. The successful synthesis and characterization of as-synthesized $NiFe_2O_4$ nanoparticles obtained by the sol-gel auto combustion method were revealed by several physical methods such as XRD, FTIR, SEM, Particle and Zeta Sizer, STA, VSM, and UV–Visible spectrophotometer. The thermal treatment at distinct temperatures of 400, 600, and 800 °C wields a substantial impact on various properties of $NiFe_2O_4$ with the same composition. The formation of pure cubic spinel structure of $NiFe_2O_4$ nanoparticles with crystallite sizes ranging from 28.01 to 320.97 nm was determined by XRD analysis. The FTIR spectra confirmed the formation of metal-oxygen bonds at tetrahedral (600–550 cm^{-1}) and octahedral (450-385 cm^{-1}) sites of $NiFe_2O_4$. The increment of particle sizes with sintering temperatures was revealed by SEM, along with a particle size analyzer. The combined results of TG and DSC showed the thermal behavior of the intermediate sample. A high colloidal stability dispersion medium was suggested by zeta potential measurements. The UV–visible spectra of prepared samples confirmed that the materials were visible active with the band gap energies ranging from 1.45 to 1.43 eV arised from direct transitions. The dependence of saturation magnetization, coercivity, remnant magnetization on the sintering temperature was explored by VSM. Furthermore, the as-fabricated ferromagnetic $NiFe_2O_4$ nanoparticles possess single domain, which was confirmed by the value of coercivity and squareness ratio. The catalytic activity of $NiFe_2O_4$ nanoparticles calcined at 400 °C was tested against MB, CR, and Rod B where nickel ferrite showed the best results for methylene blue due to the lowest size, large surface area and low band gap energy of the prepared sample. The obtained nanocrystalline $NiFe_2O_4$ powders were capable in speeding up the catalytic breakdown of the mentioned pollutants under visible light radiation. From these investigations, it can be concluded that the obtained results confirmed that temperature has a great impact on nickel ferrite nanoparticles and the resultant properties of $NiFe_2O_4$ compromise of potent applications in dye degradation of textile effluent.

Data availability

Data will be made available on request.

CRediT authorship contribution statement

Bristy Biswas: Writing – review & editing, Writing – original draft, Validation, Supervision, Resources, Project administration, Methodology, Investigation, Funding acquisition, Formal analysis, Conceptualization. **Md Farid Ahmed:** Writing – review & editing, Visualization, Validation, Resources. **Md Lutfor Rahman:** Writing – review & editing, Visualization, Validation, Resources. **Juliya Khanam:** Writing – review & editing, Visualization. **Md Habibur Rahman Bhuiyan:** Writing – review & editing, Visualization, Resources. **Nahid Sharmin:** Writing – review & editing, Visualization, Validation, Supervision, Resources, Project administration, Funding acquisition.

Declaration of competing interest

The authors declare that they have no known competing financial interests or personal relationships that could have appeared to influence the work reported in this paper.

Acknowledgements

The authors are grateful to Bangladesh Council of Scientific and Industrial Research (BCSIR) authority for financial support through R&D project (ref. no. February 39, 0000.011.14.157.2022/172; Date: November 10, 2022). The authors would also like to acknowledge the Ceramic Raw Materials & Ceramic Materials Testing Division, Glass Research Division, Institute of Glass and Ceramic Research & Testing (IGCRT), Strengthening of Institute of Glass and Ceramic Research & Testing (IGCRT) project (SIGCRT) of BCSIR, Institute of Energy Research & Development (IERD), BCSIR Laboratories, Dhaka and Central Analytical Research Facilities (CARF), Bangladesh Council of Scientific and Industrial Research (BCSIR), Dhaka, Bangladesh for providing technical supports.

References

[1] A. Kumar, A. Kumar, G. Sharma, A.H. Al-Muhtaseb, M. Naushad, A.A. Ghfar, C. Guo, F.J. Stadler, Biochar-templated g-C3N4/Bi2O2CO3/CoFe2O4 nano-assembly for visible and solar assisted photo-degradation of paraquat, nitrophenol reduction and CO2 conversion, Chem. Eng. J. 339 (2018) 393–410, https://doi.org/10.1016/J.CEJ.2018.01.105.

[2] C. Tang, Y. Yi, Z. Yang, X. Cheng, Water pollution risk simulation and prediction in the main canal of the South-to-North Water Transfer Project, J. Hydrol. 519 (2014) 2111–2120, https://doi.org/10.1016/j.jhydrol.2014.10.010.

[3] X. Miao, Y. Tang, C.W.Y. Wong, H. Zang, The latent causal chain of industrial water pollution in China, Environ. Pollut. 196 (2015) 473–477, https://doi.org/10.1016/j.envpol.2014.11.010.

[4] G. Muthuraman, T.T. Teng, Extraction and recovery of rhodamine B, methyl violet and methylene blue from industrial wastewater using D2EHPA as an extractant, J. Ind. Eng. Chem. 15 (2009) 841–846, https://doi.org/10.1016/j.jiec.2009.09.010.

[5] S. Kant, D. Pathania, P. Singh, P. Dhiman, A. Kumar, Removal of malachite green and methylene blue by Fe0.01Ni0.01Zn0.98O/polyacrylamide nanocomposite using coupled adsorption and photocatalysis, Appl. Catal. B Environ. 147 (2014) 340–352, https://doi.org/10.1016/j.apcatb.2013.09.001.

[6] S. Sharma, G. Sharma, A. Kumar, P. Dhiman, T.S. AlGarni, M. Naushad, Z.A. Alothman, F.J. Stadler, Controlled synthesis of porous Zn/Fe based layered double hydroxides: synthesis mechanism, and ciprofloxacin adsorption, Sep. Purif. Technol. 278 (2022) 119481, https://doi.org/10.1016/j.seppur.2021.119481.

[7] S. Natarajan, H.C. Bajaj, R.J. Tayade, Recent advances based on the synergetic effect of adsorption for removal of dyes from waste water using photocatalytic process, J. Environ. Sci. (China) 65 (2018) 201–222, https://doi.org/10.1016/j.jes.2017.03.011.

[8] V.K. Gupta, R. Kumar, A. Nayak, T.A. Saleh, M.A. Barakat, Adsorptive removal of dyes from aqueous solution onto carbon nanotubes: a review, Adv. Colloid Interface Sci. 193–194 (2013) 24–34, https://doi.org/10.1016/j.cis.2013.03.003.

[9] P. Dhiman, M. Patial, A. Kumar, M. Alam, M. Naushad, G. Sharma, D.V.N. Vo, R. Kumar, Environmental friendly and robust Mg0.5-xCuxZn0.5Fe2O4 spinel nanoparticles for visible light driven degradation of Carbamazepine: band shift driven by dopants, Mater. Lett. 284 (2021) 129005, https://doi.org/10.1016/J.MATLET.2020.129005.

[10] P. Dhiman, A. Kumar, M. Shekh, G. Sharma, G. Rana, D.V.N. Vo, N. AlMasoud, M. Naushad, Z.A. Alothman, Robust magnetic ZnO-Fe2O3 Z-scheme hetereojunctions with in-built metal-redox for high performance photo-degradation of sulfamethoxazole and electrochemical dopamine detection, Environ. Res. 197 (2021) 111074, https://doi.org/10.1016/j.envres.2021.111074.

[11] V.K. Gupta, R. Jain, A. Mittal, T.A. Saleh, A. Nayak, S. Agarwal, S. Sikarwar, Photo-catalytic degradation of toxic dye amaranth on TiO2/UV in aqueous suspensions, Mater. Sci. Eng. C 32 (2012) 12–17, https://doi.org/10.1016/j.msec.2011.08.018.

[12] J. Cevallos-Mendoza, C.G. Amorim, J.M. Rodríguez-Díaz, M. da C.B.S.M. Montenegro, Removal of contaminants from water by membrane filtration: a review, Membranes 12 (2022) 1–23, https://doi.org/10.3390/membranes12060570.

[13] A. Saravanan, P.S. Kumar, D.V.N. Vo, P.R. Yaashikaa, S. Karishma, S. Jeevanantham, B. Gayathri, V.D. Bharathi, Photocatalysis for removal of environmental pollutants and fuel production: a review, Environ. Chem. Lett. 19 (2021) 441–463, https://doi.org/10.1007/s10311-020-01077-8.

[14] J.K. Im, E.J. Sohn, S. Kim, M. Jang, A. Son, K.D. Zoh, Y. Yoon, Review of MXene-based nanocomposites for photocatalysis, Chemosphere 270 (2021) 129478, https://doi.org/10.1016/j.chemosphere.2020.129478.

[15] A. Kumar, G. Sharma, M. Naushad, A.H. Al-Muhtaseb, A. García-Peñas, G.T. Mola, C. Si, F.J. Stadler, Bio-inspired and biomaterials-based hybrid photocatalysts for environmental detoxification: a review, Chem. Eng. J. 382 (2020) 122937, https://doi.org/10.1016/j.cej.2019.122937.

[16] A. Mudhoo, S. Paliya, P. Goswami, M. Singh, G. Lofrano, M. Carotenuto, F. Carraturo, G. Libralato, M. Guida, M. Usman, S. Kumar, Fabrication, Functionalization and Performance of Doped Photocatalysts for Dye Degradation and Mineralization: a Review, Springer International Publishing, 2020, https://doi.org/10.1007/s10311-020-01045-2.

[17] M. Aqeel, M. Rashid, M. Ikram, A. Haider, S. Naz, J. Haider, A. Ul-Hamid, A. Shahzadi, Photocatalytic, dye degradation, and bactericidal behavior of Cu-doped ZnO nanorods and their molecular docking analysis, Dalton Trans. 49 (2020) 8314–8330, https://doi.org/10.1039/d0dt01397h.

[18] K. Subramanyam, N. Sreelekha, D.A. Reddy, M. Ramanadha, B. Poornaprakash, K.C. Reddy, R.P. Vijayalakshmi, Influence of transition metals co-doping on CeO2 magnetic and photocatalytic activities, Ceram. Int. 46 (2020) 5086–5097, https://doi.org/10.1016/j.ceramint.2019.10.252.

[19] H. Karimi-Maleh, C.T. Fakude, N. Mabuba, G.M. Peleyeju, O.A. Arotiba, The determination of 2-phenylphenol in the presence of 4-chlorophenol using nano-Fe3O4/ionic liquid paste electrode as an electrochemical sensor, J. Colloid Interface Sci. 554 (2019) 603–610, https://doi.org/10.1016/j.jcis.2019.07.047.

[20] M. Sun, H. Xu, A novel application of plasmonics: plasmon-driven surface-catalyzed reactions, Small 8 (2012) 2777–2786, https://doi.org/10.1002/smll.201200572.

[21] L. Cui, P. Wang, Y. Fang, Y. Li, M. Sun, A plasmon-driven selective surface catalytic reaction revealed by surface-enhanced Raman scattering in an electrochemical environment, Sci. Rep. 5 (2015) 1–10, https://doi.org/10.1038/srep11920.

[22] S. Duan, R. Wang, Au/Ni12P5 core/shell nanocrystals from bimetallic heterostructures: in situ synthesis, evolution and supercapacitor properties, NPG Asia Mater. 6 (2014) e122, https://doi.org/10.1038/am.2014.65.

[23] F. Moradnia, S. Taghavi Fardood, A. Ramazani, V.K. Gupta, Green synthesis of recyclable MgFeCrO4 spinel nanoparticles for rapid photodegradation of direct black 122 dye, J. Photochem. Photobiol. Chem. 392 (2020) 112433, https://doi.org/10.1016/j.jphotochem.2020.112433.

[24] R. Rameshbabu, B. Neppolian, Surfactant assisted hydrothermal synthesis of superparamagnetic ZnFe2O4 nanoparticles as an efficient visible-light photocatalyst for the degradation of organic pollutant, J. Cluster Sci. 27 (2016) 1977–1987, https://doi.org/10.1007/s10876-016-1057-0.

[25] D. Chahar, S. Taneja, S. Bisht, S. Kesarwani, P. Thakur, A. Thakur, P.B. Sharma, Photocatalytic activity of cobalt substituted zinc ferrite for the degradation of methylene blue dye under visible light irradiation, J. Alloys Compd. 851 (2021) 156878, https://doi.org/10.1016/j.jallcom.2020.156878.

[26] A. Behera, D. Kandi, S. Mansingh, S. Martha, K. Parida, Facile synthesis of ZnFe2O4@RGO nanocomposites towards photocatalytic ciprofloxacin degradation and H2 energy production, J. Colloid Interface Sci. 556 (2019) 667–679, https://doi.org/10.1016/j.jcis.2019.08.109.

[27] F. Mohammad A. Alzahrani, A. Farooq, M. Anwar, Z.A. Alrowaili, M.S. Al-Buriahi, M. Farooq Warsi, Synthesis and characterization of rGO based nanocomposite of doped nickel ferrite for outstanding photodegradation of industrial effluents, Mater. Sci. Eng. B 302 (2024) 117255, https://doi.org/10.1016/J.MSEB.2024.117255.

[28] M. Mousavi, A. Habibi-Yangjeh, Magnetically recoverable highly efficient visible-light-active g-C3N4/Fe3O4/Ag2WO4/AgBr nanocomposites for photocatalytic degradations of environmental pollutants, Adv. Powder Technol. 29 (2018) 94–105, https://doi.org/10.1016/j.apt.2017.10.016.

[29] J. Luo, X. Zhou, L. Ma, X. Xu, And coupling with CeO2 for the degradation of methyl orange under visible light irradiationEnhancing visible-light photocatalytic activity of g-C3N4 by doping phosphorus, RSC Adv. 5 (2015) 68728–68735, https://doi.org/10.1039/c5ra10848a.

[30] Y. Li, T. Wu, K. Jin, Y. Qian, N. Qian, K. Jiang, W. Wu, G. Tong, Controllable synthesis and enhanced microwave absorbing properties of Fe 3 O 4/NiFe 2 O 4/Ni heterostructure porous rods, Appl. Surf. Sci. 387 (2016) 190–201, https://doi.org/10.1016/j.apsusc.2016.06.103.

[31] M. Srivastava, A.K. Ojha, S. Chaubey, J. Singh, In-situ synthesis of magnetic (NiFe2O4/CuO/FeO) nanocomposites, J. Solid State Chem. 183 (2010) 2669–2674, https://doi.org/10.1016/j.jssc.2010.08.037.

[32] S. Mahalingam, Y.H. Ahn, Improved visible light photocatalytic activity of rGO-Fe3O4-NiO hybrid nanocomposites synthesized by: in situ facile method for industrial wastewater treatment applications, New J. Chem. 42 (2018) 4372–4383, https://doi.org/10.1039/c8nj00013a.

[33] S. Sagadevan, Z.Z. Chowdhury, R.F. Rafique, Preparation and characterization of nickel ferrite nanoparticles via co-precipitation method, Mater. Res. 21 (2018) 21–25, https://doi.org/10.1590/1980-5373-mr-2016-0533.

[34] K.K. Kefeni, B.B. Mamba, Photocatalytic application of spinel ferrite nanoparticles and nanocomposites in wastewater treatment: review, Sustain. Mater. Technol. 23 (2020) e00140, https://doi.org/10.1016/J.SUSMAT.2019.E00140.

[35] C. Xiangfeng, J. Dongli, Z. Chenmou, The preparation and gas-sensing properties of NiFe2O4 nanocubes and nanorods, Sensor. Actuator. B Chem. 123 (2007) 793–797, https://doi.org/10.1016/j.snb.2006.10.020.

[36] K.M. Lee, C.W. Lai, K.S. Ngai, J.C. Juan, Recent Developments of Zinc Oxide Based Photocatalyst in Water Treatment Technology: A Review, Elsevier Ltd, 2016, https://doi.org/10.1016/j.watres.2015.09.045.

[37] A. Nadumane, K. Shetty, K.S. Anantharaju, H.P. Nagaswarupa, D. Rangappa, Y.S. Vidya, H. Nagabhushana, S.C. Prashantha, Sunlight photocatalytic performance of Mg-doped nickel ferrite synthesized by a green sol-gel route, J. Sci. Adv. Mater. Devices 4 (2019) 89–100, https://doi.org/10.1016/j.jsamd.2018.12.002.
[38] M.R. Phadatare, A.B. Salunkhe, V.M. Khot, C.I. Sathish, D.S. Dhawale, S.H. Pawar, Thermodynamic, structural and magnetic studies of NiFe2O4 nanoparticles prepared by combustion method: effect of fuel, J. Alloys Compd. 546 (2013) 314–319, https://doi.org/10.1016/J.JALLCOM.2012.08.092.
[39] M. Mozaffari, J. Amighian, E. Darsheshdar, Magnetic and structural studies of nickel-substituted cobalt ferrite nanoparticles, synthesized by the sol-gel method, J. Magn. Magn Mater. 350 (2014) 19–22, https://doi.org/10.1016/j.jmmm.2013.08.008.
[40] S. Zare, A.A. Ati, S. Dabagh, R.M. Rosnan, Z. Othaman, Synthesis, structural and magnetic behavior studies of Zn–Al substituted cobalt ferrite nanoparticles, J. Mol. Struct. 1089 (2015) 25–31, https://doi.org/10.1016/J.MOLSTRUC.2015.02.006.
[41] X. Wu, Z. Ding, N. Song, L. Li, W. Wang, Effect of the rare-earth substitution on the structural, magnetic and adsorption properties in cobalt ferrite nanoparticles, Ceram. Int. 42 (2016) 4246–4255, https://doi.org/10.1016/j.ceramint.2015.11.100.
[42] M. Dhiman, A. Goyal, V. Kumar, S. Singhal, Designing different morphologies of NiFe2O4 for tuning of structural, optical and magnetic properties for catalytic advancements. https://doi.org/10.1039/c6nj03209e, 2016.
[43] S.Q. Liu, L.R. Feng, N. Xu, Z.G. Chen, X.M. Wang, Magnetic nickel ferrite as a heterogeneous photo-Fenton catalyst for the degradation of rhodamine B in the presence of oxalic acid, Chem. Eng. J. 203 (2012) 432–439, https://doi.org/10.1016/j.cej.2012.07.071.
[44] M.K.A. Kar, R. Fazaeli, F. Manteghi, M. Ghahari, Elimination of direct red 264 using magnetic pure and Zn-doped NiFe2O4 nanophotocatalysts under visible light irradiation: isothermic and kinetic studies, Environ. Prog. Sustain. Energy 38 (2019) 1–10, https://doi.org/10.1002/ep.13097.
[45] T.P. Oliveira, G.N. Marques, M.A. Macedo Castro, R.C. Viana Costa, J.H.G. Rangel, S.F. Rodrigues, C.C. dos Santos, M.M. Oliveira, Synthesis and photocatalytic investigation of ZnFe2O4 in the degradation of organic dyes under visible light, J. Mater. Res. Technol. 9 (2020) 15001–15015, https://doi.org/10.1016/j.jmrt.2020.10.080.
[46] V.A.F. Samson, S.B. Bernadsha, M. Mahendiran, K.L. Lawrence, J. Madhavan, M.V.A. Raj, S. Prathap, Impact of calcination temperature on structural, optical, and magnetic properties of spinel CuFe2O4 for enhancing photocatalytic activity, J. Mater. Sci. Mater. Electron. 31 (2020) 6574–6585, https://doi.org/10.1007/s10854-020-03213-0.
[47] N.T.T. Loan, N.T.H. Lan, N.T. Thuy Hang, N.Q. Hai, D.T.T. Anh, V.T. Hau, L. Van Tan, T. Van Tran, CoFe2O4 nanomaterials: effect of annealing temperature on characterization, magnetic, photocatalytic, and photo-fenton properties, Processes 7 (2019) 1–14, https://doi.org/10.3390/PR7120885.
[48] S. Shokri, N. Shariatifar, E. Molaee-Aghaee, G.J. Khaniki, P. Sadighara, M.A. Faramarzi, M. Mohammadi, A. Rezagholizade-shirvan, Synthesis and characterization of a novel magnetic chitosan–nickel ferrite nanocomposite for antibacterial and antioxidant properties, Sci. Rep. 13 (2023) 1–12, https://doi.org/10.1038/s41598-023-42974-6.
[49] J. Khanam, M.R. Hasan, B. Biswas, S.A. Jahan, N. Sharmin, S. Ahmed, S.M. Al-Reza, Development of ceramic grade red iron oxide pigment from waste iron source, Heliyon 9 (2023) e12854, https://doi.org/10.1016/j.heliyon.2023.e12854.
[50] M. Podder, M. Rassel Moni, M. Lutfor Rahman, B. Biswas, N. Sharmin, M. Hakim, M. Rahman, M. Sahadat Hossain, M. Farid Ahmed, Exploration of properties (crystallographic, morphological, optical) of nano cobalt aluminate synthesized by facile sol–gel method: effects of sintering temperature, Arab. J. Chem. 17 (2024) 105601, https://doi.org/10.1016/j.arabjc.2024.105601.
[51] V.A. Bharati, S.R. Patade, S. Bajaj, R. Parlikar, A.P. Keche, V.V. Sondur, Structural and magnetic properties of nickel ferrite nanoparticles prepared by solution combustion method, J. Phys. Conf. Ser. 1644 (2020), https://doi.org/10.1088/1742-6596/1644/1/012005.
[52] N.K. Das, J. Chakrabartty, S.F.U. Farhad, A.K. Sen Gupta, E.M.K. Ikball Ahamed, K.S. Rahman, A. Wafi, A.A. Alkahtani, M.A. Matin, N. Amin, Effect of substrate temperature on the properties of RF sputtered CdS thin films for solar cell applications, Results Phys. 17 (2020) 103132, https://doi.org/10.1016/j.rinp.2020.103132.
[53] M. Basak, M.L. Rahman, M.F. Ahmed, B. Biswas, N. Sharmin, Calcination effect on structural, morphological and magnetic properties of nano-sized CoFe2O4 developed by a simple co-precipitation technique, Mater. Chem. Phys. 264 (2021) 124442, https://doi.org/10.1016/j.matchemphys.2021.124442.
[54] M. Gharagozlou, Synthesis, characterization and influence of calcination temperature on magnetic properties of nanocrystalline spinel Co-ferrite prepared by polymeric precursor method, J. Alloys Compd. 486 (2009) 660–665, https://doi.org/10.1016/j.jallcom.2009.07.025.
[55] E. Suharyadi, S.H. Pratiwi, I.P. Tedy Indrayana, T. Kato, S. Iwata, K. Ohto, Effects of annealing temperature on microstructural, magnetic properties, and specific absorption rate of Zn-Ni ferrite nanoparticles, Mater. Res. Express 8 (2021), https://doi.org/10.1088/2053-1591/abe986.
[56] S. Singh, A.K. Atri, I. Qadir, S. Sharma, U. Manhas, D. Singh, Role of different fuels and sintering temperatures in the structural, optical, magnetic, and photocatalytic properties of chromium-containing nickel ferrite: kinetic study of photocatalytic degradation of rhodamine B dye, ACS Omega 8 (2023) 6302–6317, https://doi.org/10.1021/acsomega.2c06249.
[57] M. Podder, M.F. Ahmed, M.R. Moni, M.L. Rahman, B. Biswas, N. Sharmin, Effect of metal ions on structural, morphological and optical properties of nanocrystallite spinel cobalt-aluminate (CoAl2O4), Arab. J. Chem. 16 (2023) 104700, https://doi.org/10.1016/j.arabjc.2023.104700.
[58] M. Rahman, M. Lutfor Rahman, B. Biswas, M. Farid Ahmed, M. Aftab Ali Shaikh, S. Akter Jahan, N. Sharmin, Effect of Ni-doping on coloring and photocatalytic performance of MgTi2O5 nanoceramics, J. Ind. Eng. Chem. 126 (2023) 340–359, https://doi.org/10.1016/J.JIEC.2023.06.024.
[59] V. Kumar, N. Kumar, S. Bhushan Das, R.K. Singh, K. Sarkar, M. Kumar, Sol-gel assisted synthesis and tuning of structural, photoluminescence, magnetic and multiferroic properties by annealing temperature in nanostructured zinc ferrite, Mater. Today Proc. 47 (2021) 6242–6248, https://doi.org/10.1016/j.matpr.2021.05.215.
[60] S. Da Dalt, A.S. Takimi, T.M. Volkmer, V.C. Sousa, C.P. Bergmann, Magnetic and Mössbauer behavior of the nanostructured MgFe2O4 spinel obtained at low temperature, Powder Technol. 210 (2011) 103–108, https://doi.org/10.1016/j.powtec.2011.03.001.
[61] S. Swathi, R. Yuvakkumar, P.S. Kumar, G. Ravi, D. Velauthapillai, Annealing temperature effect on cobalt ferrite nanoparticles for photocatalytic degradation, Chemosphere 281 (2021) 130903, https://doi.org/10.1016/J.CHEMOSPHERE.2021.130903.
[62] M. Saha, S. Mukherjee, S. Kumar, S. Dey, A. Gayen, Albumin matrix assisted wet chemical synthesis of nanocrystalline MFe2O4 (M = Cu, Co and Zn) ferrites for visible light driven degradation of methylene blue by hydrogen peroxide, RSC Adv. 6 (2016) 58125–58136, https://doi.org/10.1039/c6ra04825k.
[63] H. Moradmard, S. Farjami Shayesteh, P. Tohidi, Z. Abbas, M. Khaleghi, Structural, magnetic and dielectric properties of magnesium doped nickel ferrite nanoparticles, J. Alloys Compd. 650 (2015) 116–122, https://doi.org/10.1016/j.jallcom.2015.07.269.
[64] R. Gusain, N. Kumar, S.S. Ray, Factors influencing the photocatalytic activity of photocatalysts in wastewater treatment, Photocatal. Adv. Oxid. Process. Wastewater Treat. (2020) 229–270, https://doi.org/10.1002/9781119631422.ch8.
[65] P. Dhiman, G. Rana, E.A. Dawi, A. Kumar, G. Sharma, A. Kumar, J. Sharma, Tuning the photocatalytic performance of Ni-Zn ferrite catalyst using Nd doping for solar light-driven catalytic degradation of methylene blue, Water (Switzerland) 15 (2023), https://doi.org/10.3390/w15010187.
[66] R. Jiang, H. Zhu, Y. Fu, S. Jiang, E. Zong, J. Yao, Photocatalytic decolorization of Congo red wastewater by magnetic ZnFe2O4/graphene nanosheets composite under simulated solar light irradiation, Ozone Sci. Eng. 42 (2020) 174–182, https://doi.org/10.1080/01919512.2019.1635432.
[67] A.R.B. Bayantong, Y.J. Shih, C. Di Dong, S. Garcia-Segura, M.D.G. de Luna, Nickel ferrite nanoenabled graphene oxide (NiFe2O4@GO) as photoactive nanocomposites for water treatment, Environ. Sci. Pollut. Res. 28 (2021) 5472–5481, https://doi.org/10.1007/s11356-020-10545-1.
[68] S. Munir, M. Farooq Warsi, S. Zulfiqar, I. Ayman, S. Haider, I.A. Alsafari, P.O. Agboola, I. Shakir, Nickel ferrite/zinc oxide nanocomposite: investigating the photocatalytic and antibacterial properties, J. Saudi Chem. Soc. 25 (2021) 101388, https://doi.org/10.1016/j.jscs.2021.101388.
[69] O. Cofe, M. Lotfi, M. Mirzaei, A. Hassanpour, H. Safardoust-hojaghan, Visible Light-Induced Photocatalytic Performance of Green MnFe 2 O 4 and, (n.d.).
[70] R. Jasrotia, N. Jaswal, J. Prakash, C.C. Kit, J. Singh, A. Kandwal, Photocatalytic application of magnesium spinel ferrite in wastewater remediation: a review, J. Magnesium Alloys 12 (2024) 490–505, https://doi.org/10.1016/j.jma.2024.02.006.

[71] E. Elanthamilan, I.B. Elizabeth, S.F. Wang, I.S. Lydia, Strontium hexaferrite microspheres: synthesis, characterization and visible-light-driven photocatalytic activity towards the degradation of methylene blue dye, Opt. Mater. 137 (2023) 113565, https://doi.org/10.1016/J.OPTMAT.2023.113565.
[72] P.A. Udhaya, A. Ahmad, M. Meena, M.A.J. Queen, M. Aravind, P. Velusamy, T.M. Almutairi, A.A.A. Mohammed, S. Ali, Copper Ferrite nanoparticles synthesised using a novel green synthesis route: structural development and photocatalytic activity, J. Mol. Struct. 1277 (2023) 134807, https://doi.org/10.1016/J.MOLSTRUC.2022.134807.
[73] J.R. Adarsha, T.N. Ravishankar, C.R. Manjunatha, T. Ramakrishnappa, Green synthesis of nanostructured calcium ferrite particles and its application to photocatalytic degradation of Evans blue dye, Mater. Today Proc. 49 (2021) 777–788, https://doi.org/10.1016/j.matpr.2021.05.293.